



Advances in retrieving methane and carbon monoxide from TROPOMI onboard Sentinel-5 Precursor

Oliver Schneising, Michael Buchwitz, Jonas Hachmeister, Steffen Vanselow, Maximilian Reuter, Matthias Buschmann, Heinrich Bovensmann, and John P. Burrows

Institute of Environmental Physics (IUP), University of Bremen FB1, Bremen, Germany

Correspondence: O. Schneising (oliver.schneising@iup.physik.uni-bremen.de)

Abstract. The TROPOspheric Monitoring Instrument (TROPOMI) onboard the Sentinel-5 Precursor satellite enables the accurate determination of atmospheric methane (CH_4) and carbon monoxide (CO) abundances at high spatial resolution and global daily sampling. Due to its wide swath and sampling, the global distribution of both gases can be determined in unprecedented detail. The scientific retrieval algorithm Weighting Function Modified Differential Optical Absorption Spectroscopy (WFMD) has proven valuable in simultaneously retrieving the atmospheric column-averaged dry air mole fractions XCH_4 and XCO from TROPOMI's radiance measurements in the shortwave infrared (SWIR) spectral range.

Here we present recent improvements of the algorithm which have been incorporated into the current version v1.8 of the TROPOMI/WFMD product. This includes processing adjustments such as increasing the polynomial degree to 3 in the fitting procedure to better account for possible spectral albedo variations within the fitting window and updating the digital elevation model to minimise topography related biases. In the post-processing, the machine-learning-based quality filter has been refined using additional data when training the random forest classifier to further reduce scenes with residual cloudiness that are incorrectly classified as good. Furthermore, the machine learning calibration, addressing systematic errors due to simplifications in the forward model or instrumental issues, has been optimised. To remove vertical stripes in the XCH_4 and XCO data, an efficient orbitwise destriping filter based on combined wavelet-Fourier filtering has been implemented, while optimally preserving the original spatial trace gas features. The temporal coverage of the data records has been extended to the end of April 2022 covering a total length of 4.5 years since the start of the mission and will be further extended in the future.

The improvements, which have been implemented, reduce the pseudo-noise component of the products resulting in an improved random error. The XCH_4 and XCO products have similar spatial coverage from year to year including high latitudes and the oceans. The analysis of annual growth rates reveals an accelerated growth of atmospheric methane during the covered period, in line with observations at marine surface sites of the Global Monitoring Division of NOAA's Earth System Research Laboratory, which reported consecutive annual record increases over the past two years 2020 and 2021.

1 Introduction

Methane (CH_4) is the second most important greenhouse gas released by anthropogenic activity. Although it is less abundant, it exhibits a significantly larger mass-related global warming potential than carbon dioxide (CO_2), which is responsible for



25 most of the human-induced radiative forcing since 1750 (Masson-Delmotte et al., 2021). Comprehensive knowledge of the
source and sink processes of CH₄ is essential for a reliable prediction of future climate. Since CH₄ is considerably shorter-
lived in the atmosphere (about 9 years) than CO₂, reducing methane emissions offers the opportunity to take advantage of
the corresponding short-term climate benefits to come within reach of the goal of limiting global warming to 1.5°C. In this
context, global detection and quantification of methane sources through satellite remote sensing can contribute to the emission
30 mitigation efforts by identifying main emitters of anthropogenic origin, e.g. from the energy, waste or agricultural sectors, and
thus suggesting effective emission reduction strategies.

Carbon monoxide (CO) is an air contaminant that is released into the atmosphere during combustion processes and as a
result of the oxidation of hydrocarbons. This occurs both through natural processes and resulting from human activities. CO
has adverse health effects as it impairs the oxygen-carrying capacity of the blood by directly binding to haemoglobin (Rose
35 et al., 2015). Due to its lifetime of approximately 1-2 months, it is well suited as tracer of the long-range transport of pollutants.
In the presence of sufficient NO_x, CO participates in the net production of tropospheric ozone (Fowler et al., 2008), which is a
greenhouse gas and known to be harmful to health. In addition, CO is the main sink for the hydroxyl radical (OH) reducing the
potential of atmospheric self-cleansing because the chemically depleted OH is no longer available to remove other constituents
of the atmosphere, including greenhouse gases such as methane. Consequently, CO is considered an indirect contributor to
40 climate change.

Continuous global satellite observations of both gases enable a better insight into atmospheric transport, tropospheric chem-
istry, and the climate system. Measurements of the upwelling radiances in the shortwave infrared (SWIR) spectral region have
been exploited for the retrieval of the abundances and distributions of trace gases, such as CO₂, CH₄, and CO, because they
are sensitive to all atmospheric layers. The Measurement of Pollution in the Troposphere (MOPITT) instrument (Drummond
45 et al., 2010) onboard NASA's Terra satellite successfully retrieves CO from both the thermal and shortwave infrared and was
intended to measure CH₄. The SCanning Imaging Absorption spectroMeter for Atmospheric CHartographY (SCIAMACHY)
(Burrows et al., 1995; Bovensmann et al., 1999) onboard ESA's ENVISAT began simultaneous measurements of CO₂, CH₄,
and CO from space (Buchwitz et al., 2005; Frankenberg et al., 2006). The Thermal And Near infrared Sensor for carbon Ob-
servations Fourier Transform Spectrometer (TANSO-FTS) onboard GOSAT (Kuze et al., 2016) retrieves CO₂ and CH₄, its
50 successor TANSO-FTS-2 onboard GOSAT-2 (Suto et al., 2021) additionally measures CO due to an extended spectral range.
The previously existing application areas of satellite data were further expanded with the TROPOspheric Monitoring Instru-
ment (TROPOMI), which is considered groundbreaking for determining atmospheric composition, including CH₄ and CO,
from space with respect to combined spatio-temporal coverage and data quality.

TROPOMI is the only payload instrument of the ESA Sentinel-5 Precursor mission launched in October 2017 (Veefkind
55 et al., 2012). It is a pushbroom imaging spectrometer measuring radiances in eight spectral bands from the ultraviolet (UV) to
the shortwave infrared (SWIR) allowing the retrieval of various atmospheric constituents. TROPOMI has the unique ability to
combine observations at high spatial resolution with global coverage on a daily basis due to its large 2600 km swath consisting
of individual measurements with a footprint size of 5.5 × 7 km² at nadir (7 × 7 km² before 6 August 2019) in the SWIR bands
(7 and 8) relevant for the methane and carbon monoxide retrieval. As a consequence, both gases can be detected worldwide in



60 unprecedented detail. If desired, the globally available TROPOMI data may be complemented in a symbiotic way by targeted remote sensing data from aircraft or satellites with higher spatial resolution but limited coverage, e.g. from GHGSat (Cusworth et al., 2021), to detect and identify significant emitters.

In addition to the operational TROPOMI products for CH₄ (Hu et al., 2016) and CO (Landgraf et al., 2016), there is also a scientific methane product based on the same algorithm as the operational product but with optimised settings (Lorente et al., 65 2021), as well as the scientific WFMD product providing both gases simultaneously retrieved from the same fitting window (Schneising et al., 2019). The scientific products have turned out to be valuable in verifying or improving the operational products and in assessing the robustness of results by analysing the extent to which specific results are sensitive to the details of the algorithm setup (Buchwitz et al., 2017).

Here we introduce the recent changes incorporated in the latest product version of TROPOMI/WFMD. After a short review 70 of the basics of the retrieval algorithm including machine learning quality filter and bias correction, the following sections describe in detail the improvements implemented in the current version and demonstrate their benefits. Finally, an overview of the new improved products is provided including a discussion of atmospheric annual growth rates and validation results compared to previous product versions.

2 TROPOMI/WFMD retrieval algorithm

75 The scientific retrieval algorithm Weighting Function Modified DOAS (WFMD) for simultaneously retrieving the atmospheric column-averaged dry air mole fractions of methane (XCH₄) and carbon monoxide (XCO) from radiance measurements in the SWIR of the TROPOMI instrument onboard the Sentinel-5 Precursor satellite (S5P) is described in detail in Schneising et al. (2019). It is a least-squares procedure using scaling (or shifting) of previously selected atmospheric vertical profiles (Buchwitz et al., 2007; Schneising et al., 2011). The linearised radiative transfer model (based on the tabulation of radiances and associated 80 derivatives obtained from the radiative transfer model SCIATRAN (Rozanov et al., 2002, 2014)) is fitted together with a low degree polynomial to the logarithm of the measured sun-normalised radiance. The look-up table enables a fast retrieval of the vertical columns of the targeted species and contains various reference spectra characterising a variety of typical atmospheric conditions covering combinations of different solar zenith angles, altitudes, albedos, water vapour contents, and temperatures.

Given the number $m \in \mathbb{N}$ of spectral points to be fitted and the number $n \in \mathbb{N}$ of state vector elements (with $m \gg n$), the 85 best fit of the linearised model to the observed radiance is obtained by minimising

$$f(\mathbf{x}) = \left\| \mathbf{W}^{\frac{1}{2}} (\mathbf{y} - \mathbf{A}\mathbf{x}) \right\|_2^2 = (\mathbf{y} - \mathbf{A}\mathbf{x})^T \mathbf{W} (\mathbf{y} - \mathbf{A}\mathbf{x}) \quad (1)$$

with respect to the difference $\mathbf{x} \in \mathbb{R}^n$ of the state vector and the multidimensional linearisation point. Here $\mathbf{y} \in \mathbb{R}^m$ is the corresponding difference vector of measurement and linearised model, $\mathbf{A} \in \mathbb{R}^{m \times n}$ is the Jacobian (matrix of weighting functions, i.e. derivatives at the linearisation point, and polynomial basis functions as columns), and $\mathbf{W} = \mathbf{C}_y^{-1}$ the matrix of weights 90 defined as the inverse of the measurement noise covariance matrix $\mathbf{C}_y = \text{diag}(\sigma_1^2, \dots, \sigma_m^2) \in \mathbb{R}^{m \times m}$ associated with uncorrelated measurement noise σ_i at the different spectral points. This minimisation yields the solution $\hat{\mathbf{x}} = \mathbf{C}_x \mathbf{A}^T \mathbf{W} \mathbf{y}$ of the inverse problem, with $\mathbf{C}_x = (\mathbf{A}^T \mathbf{W} \mathbf{A})^{-1}$ being the covariance matrix of solution $\hat{\mathbf{x}}$.



In post-processing, the retrieved vertical columns are converted to column-averaged dry air mole fractions (denoted X_{CH_4} and X_{CO}) by dividing them by the dry air columns obtained from European Centre for Medium-Range Weather Forecasts (ECMWF) data. To adopt the high spatial resolution of the TROPOMI data, the ECMWF dry air columns are adjusted for the actual elevation of the individual satellite scenes by accounting for the mismatch to the mean altitude of the coarser model grid.

As the look-up table is confined to specific atmospheric conditions such as cloud-free scenes, an efficient machine learning quality filtering procedure based on a random forest classifier (Schneising et al., 2019) is trained using quasi-simultaneous cloud information from the Visible Infrared Imaging Radiometer Suite (VIIRS) onboard Suomi NPP (Hutchison and Cracknell, 2005) flying in a constellation 3.5 minutes ahead of the Sentinel-5 Precursor. Due to the strict quality requirements for retrieving atmospheric methane, a shallow learning random forest regressor (shallow refers here to the number of leaves in each decision tree being small compared to the cardinality of the training dataset) is trained to reduce the remaining systematic coarse-scaled methane dependencies on other parameters such as albedo after quality filtering by assuming the Simple cLImatological Model for atmospheric CH_4 (SLIMCH4) v2021 (Noël et al., 2022) without interpolation as a sound low-resolution ($6^\circ \times 4^\circ$) approximation of truth. This correction only compensates for gross statistical discrepancies regarding the considered features (mainly albedo-related), as the tree growing is limited and the training is restricted to a subperiod of time and a few small regions, which are selected to cover the whole range of albedo values and all possible viewing geometries. Therefore, the training data set is considered representative of the entire globe with respect to albedo-related biases, ensuring a reliable global correction. The additional pruning of the decision trees is performed to keep the correction as simple, fast, and shallow as possible to be certain that potential specifics of the climatology are not over-learned.

3 Algorithm improvements

Since version v1.2 (Schneising et al., 2019), several changes have been implemented in the WFMD algorithm, which are described in this section. Besides rather straightforward adjustments, such as increasing the resolution of the used topography database from 0.05° to 0.025° and using the ECMWF Reanalysis v5 (ERA5, with resolution $0.25^\circ \times 0.25^\circ \times 1h$) (Hersbach et al., 2020) instead of the ECMWF analysis ($0.75^\circ \times 0.75^\circ \times 6h$) in the post-processing since v1.5, the more comprehensive improvements are described in the following subsections.

3.1 Polynomial fit parameters

In the original settings a quadratic function (polynomial of degree 2) was used in the minimisation procedure of (1) to take broadband effects into account when fitting the linearised radiative transfer model to the observed radiance. However, it has been noted that in rare cases suspect signals were retrieved over areas exhibiting special surface characteristics. This finding was attributed to the variability of spectral albedo within the used fitting window around $2.3\mu m$ for specific soil types depending on their exact chemical composition. Potential interferences in this spectral range could be, for example, spectral features due to OH-metal bend and OH stretch combinations (Tayebi et al., 2017) or features caused by combination tones of certain salts and gypsum (Moreira et al., 2014).

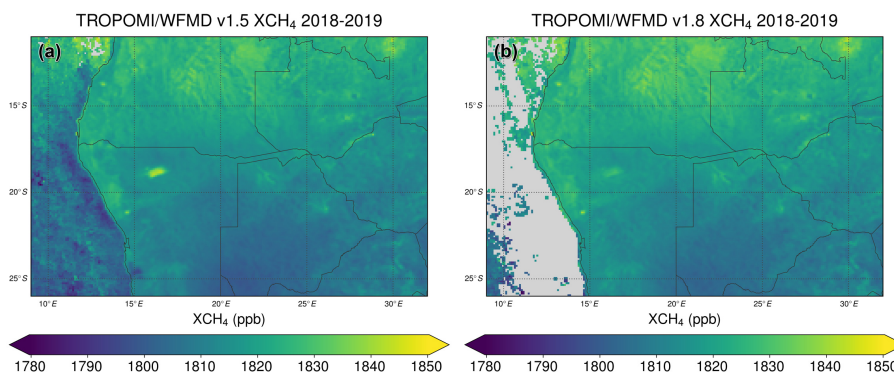


Figure 1. Comparison of the XCH₄ distribution over Southern Africa for (a) v1.5 and (b) v1.8 using a polynomial of degree 3 (instead of 2) in the fitting procedure to better account for potential variability of spectral albedo within the fitting window. As a consequence, the enhancement over the Etosha pan in Namibia is significantly reduced to a more realistic level. The differences in coverage over the ocean are due to the stricter quality filter in v1.8 (see Section 3.3).

125 The most prominent potential bias was observed over the Etosha Pan, which is a large endorheic salt pan in Namibia. It exhibits intermittent shallow inundation and is therefore considered a wetland and thus a potential methane source. After the infiltrated water has evaporated again, a salt crust remains on the ground. According to Beugler-Bell and Buch (1997), the soils of the Etosha Pan are calci sodic Solonchaks to sali calcic Solonetz derived from Andoni sandstone or siltstone, which may result in an overestimation of the detected methane enhancement, if the fitted quadratic polynomial is not able to approximate

130 the spectral albedo of this specific soil type sufficiently well. Therefore, the polynomial degree in the fitting procedure of v1.8 was increased to 3 to better account for possible spectral albedo variations within the fitting window. As a result, the enhancement over the Etosha pan in Namibia is significantly reduced to a more realistic level (see Figure 1), while other spatial features are preserved. Hence, the modification of the polynomial degree in v1.8 is considered a general improvement, with positive effects in the presence of specific soil types and otherwise no significant changes compared to previous product

135 versions. Verification with an experimental interim version has confirmed that the observed reduction over the Etosha Pan is indeed due to the increased polynomial degree and not to the other implemented changes in v1.8.

This improvement is also corroborated by the fact that the link between inundation and methane enhancement appears more evident in the latest product version. Whereas a positive signal corresponding to the extent of the pan was visible virtually every day in previous versions, the enhancement is now more pronounced when parts of the pan are shallowly flooded, as opposed

140 to days with utter drainage. This is demonstrated in Figure 2 by comparison with VIIRS true colour reflectances.

3.2 Digital elevation model

The previously used Digital Elevation Model (DEM) Global Multi-Resolution Terrain Elevation Data 2010 (GMTED2010) (United States Geological Survey, 2018) was replaced in WFMD v1.8 as significant local inaccuracies were identified over Greenland compared to ICESat-2 data (Hachmeister et al., 2022). The associated analysis confirmed the expected linear corre-

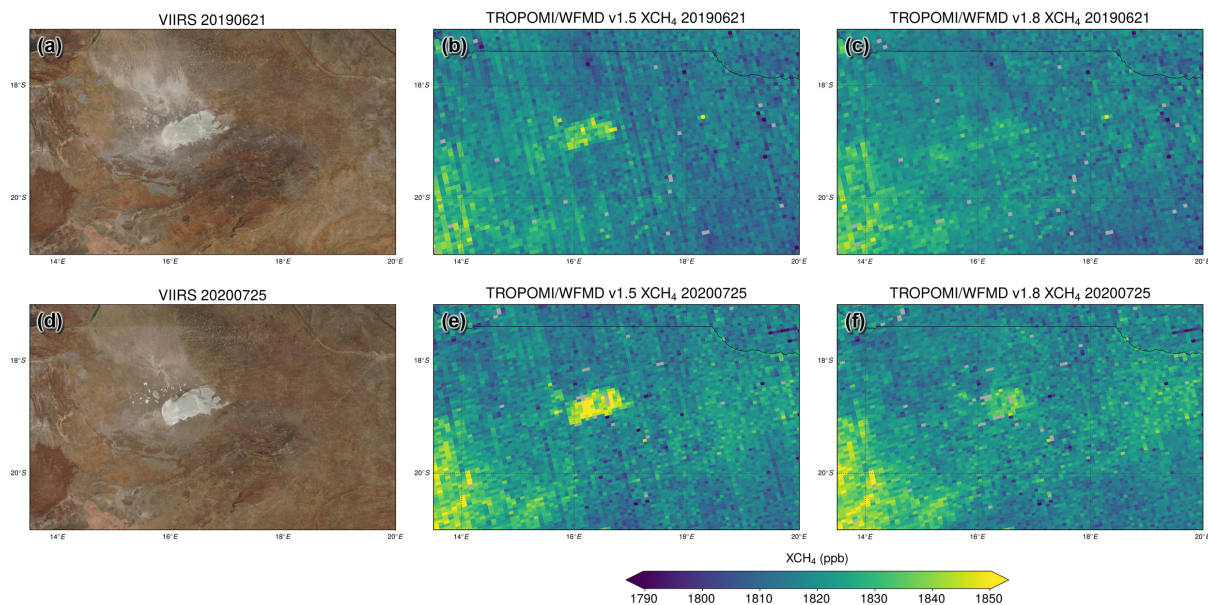


Figure 2. Comparison of (a,d) VIIRS true colour reflectances (taken from the NASA Worldview application) with the XCH₄ distribution over the Etosha pan for (b,e) v1.5 and (c,f) v1.8 on two different days (a-c) without and (d-f) with shallow inundation of parts of the pan. In the latter case there is a perceivable enhancement in the swamped portion for v1.8, which does not arise on the drained day. Please note that for v1.8 an additional destriping algorithm has been applied (see Section 3.4).

145 lation between Δh and ΔXCH_4 . Thereby, an error of 1% in the assumed surface pressure corresponds approximately to an error of 1% in retrieved XCH₄. As a universally consistent current DEM is preferable in the case of a global satellite dataset and inaccuracies of GMTED2010 could also affect other regions of the globe, the Copernicus GLO-90 DEM (European Space Agency, 2021) was utilised in the updated product instead to minimise topography related biases in the TROPOMI/WFMD XCH₄ and XCO data.

150 The freely available Copernicus GLO-90 DEM is based on radar satellite data collected between 2011-2015 during the TanDEM-X Mission and represents the full global landmass including buildings, infrastructure and vegetation at a resolution of 90m. A global validation with ICESat-1 data provides an average vertical accuracy of 2.17m at 90% confidence level (Airbus, 2020). In this global assessment, Greenland and Antarctica were excluded from the statistics due to the additional uncertainties associated with snow and ice cover. Broken down by ecoregion, the accuracy for most surface types is better
155 than 2m, while tundra, boreal forests, and woodlands have the lowest accuracy levels compared to other regions. This lower accuracy is expected because the penetration depths of radar and lidar differ for regions covered with conifers. A similar penetration depth issue exists for dry firm snow hampering a direct comparison with ICESat-1 data for regions with permanent snow or ice cover leading to lower accuracy levels in these regions. Consequently, the obtained vertical accuracies for Greenland and Antarctica are about three times higher than for the global assessment (7.26m and 6.38m at 90% confidence level).

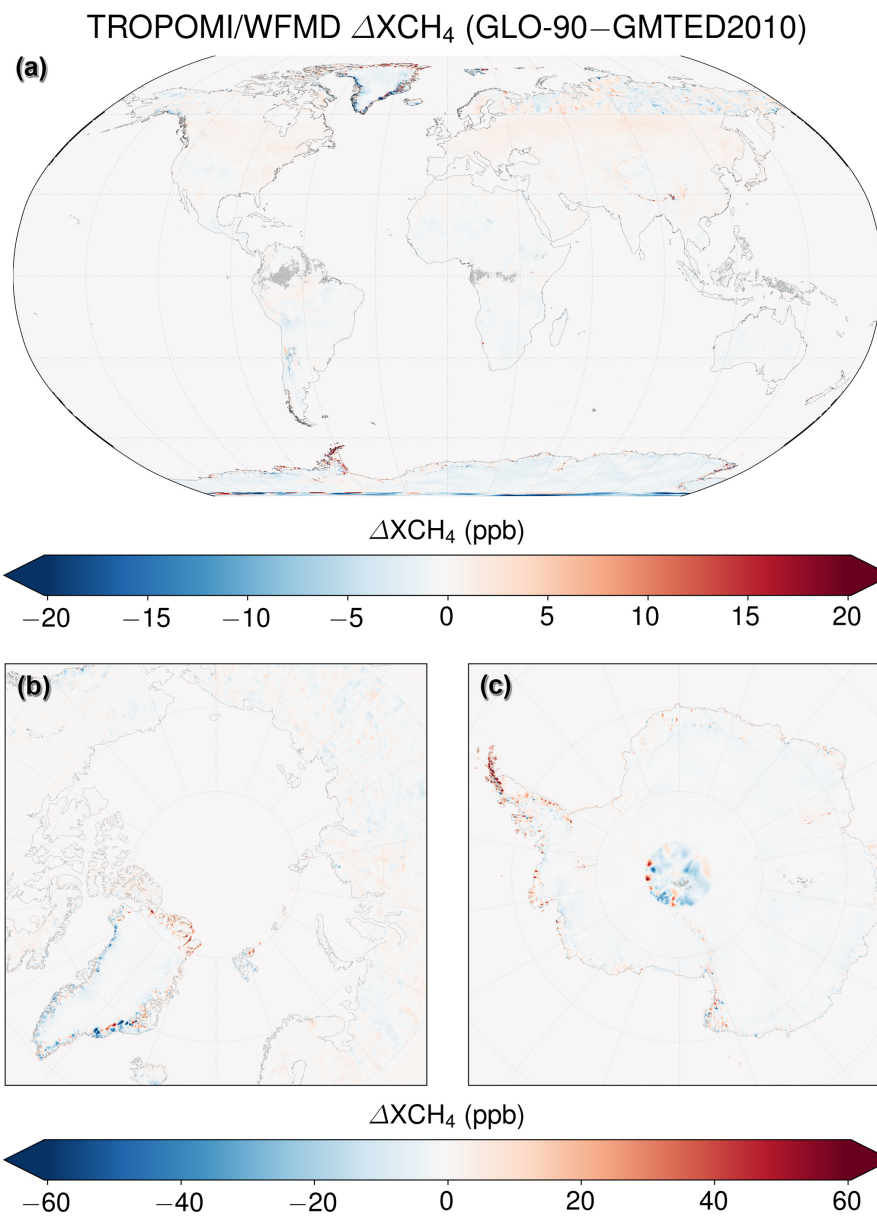


Figure 3. Global differences (a) in XCH_4 when substituting the GMTED2010 digital elevation model with GLO-90. The largest differences are in the (b) Arctic, in particular Greenland, and (c) Antarctica.

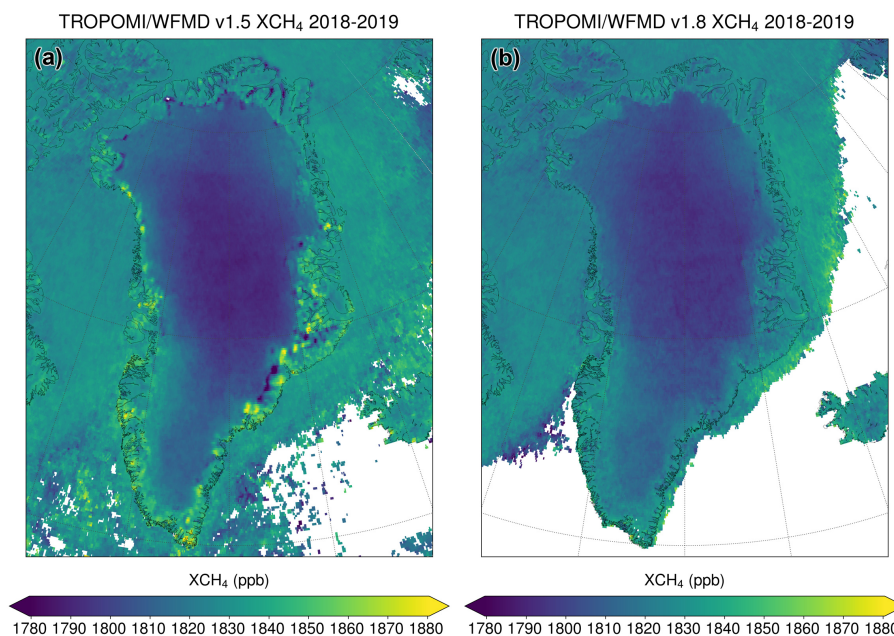


Figure 4. Comparison of the XCH₄ distribution over Greenland for (a) v1.5 based on GMTED2010 and (b) v1.8 using updated topography. The suspicious features, which are correlated with the topography-related differences shown in Figure 3, disappear when using the GLO-90 digital elevation model. The differences in coverage over the ocean are due to the stricter quality filter in v1.8 (see Section 3.3).

160 To get an idea of the impact of the DEM change, Figure 3 shows the average difference in XCH₄ when substituting
GMTED2010 with GLO-90. As can be seen, the differences are rather small for most regions of the world, but can become
large at individual locations, e.g. in Arctic regions (parts of Greenland and Spitsbergen) or Antarctica, where biases associated
with singular DEM inaccuracies of a few 100m could exceed 100ppb before the DEM change. The well-known Greenland
issue (Hachmeister et al., 2022) and the improvement through the use of GLO-90 is demonstrated in Figure 4. The updated
165 product features a more consistent and realistic methane distribution. There are similar percentage improvements for the XCO
product, but the previous inaccuracies were less significant due to the higher variability of XCO and the lower requirements
on the product compared to XCH₄.

3.3 Quality filter and posterior correction

The TROPOMI/WFMD algorithm uses machine learning in the post-processing to predict low-quality scenes and to calibrate
170 the methane retrievals by learning statistical relationships. In addition to the dedicated changes to the settings in the machine
learning framework described in this section, further effective improvements may arise if the actual underlying systematic
dependencies are better teased out due to the other refinements, such as improved topography or updated polynomial degree.



3.3.1 Machine learning quality filter

For the fastest possible Level 1 to Level 2 processing, the look-up table of radiances and their derivatives with respect to the state vector elements should be kept appropriately small. As a consequence, some assumptions and simplifications concerning atmospheric conditions have to be made resulting in the need to exclude measurements that are not adequately represented by the forward model. This primarily applies to cloudy scenes, which have to be rigorously filtered out, as the look-up table is limited to cloud-free conditions. To this end, a random forest classifier based on machine learning was implemented in the post-processing exploiting concurrent cloud information from the VIIRS instrument (Schneising et al., 2019). After the initial training, the algorithm is independent of the availability or consistency of the VIIRS data, as the classification is then entirely driven by intrinsic parameters available from or used in the preceding processing excluding the primary retrieval parameters XCH_4 and XCO .

To optimise coverage and quality of the products, the dataset used in the training of the random forest quality screening was extended to 30 days since v1.5 (compared to the original 16 days). Furthermore, surface roughness was included as an additional feature of the classifier to allow better identification of scenes that may have quality deficits due to the simplifications of the forward model. These changes result in fewer residual outliers remaining after quality filtering.

To further reduce potential outliers another 3-step quality filter was additionally implemented (since v1.5) after application of the random forest classifier: 1) Retrievals whose shift and squeeze parameters exceed the 3σ -range centred around the respective daily mean values are discarded. 2) An empirical filter with respect to the root mean square of the fit residual f_{RMS} is applied depending on the sun-normalised radiance in a spectral range with negligible absorption I_0 at the edge of the fitting window. The quality is considered bad if $f_{RMS} > 0.027$ or $f_{RMS} > a \cdot (I_0 + b)^{-1} + c$ with parameters $a = 0.0019$, $b = 0.075$, $c = 0.007$, which are adjusted for scenes over ocean and inland water (i.e. with land fraction zero) to $a = 0.00063$, $b = 0.015$, $c = 0.009$. This filter step serves, for instance, to filter out specific desert scenes with intense aerosol exposure, which leads to reduced fit quality despite the high reflectance of sand. 3) Unsupervised outlier detection is applied on daily data based on the comparison of the local density of a sample with the local densities of its neighbours. This is done by assigning a degree of being an outlier to each object in multidimensional space, called the Local Outlier Factor (LOF) (Breunig et al., 2000). It is local in the sense that the LOF depends on how isolated an object is from its surroundings, with LOF being close to 1 for objects inside a cluster. Here we use the 3-dimensional (latitude, longitude, XCH_4)-space and the standard Euclidean metric to measure the spatial distance. Thereby, any upward outliers regarding XCH_4 are not filtered out to avoid incorrectly excluding genuine emission point sources. The full 3-step procedure removes a further 3.5% of the scenes that pass the random forest classifier quality screening algorithm, with about 3% of the data filtered out by the shift/squeeze/ f_{RMS} -Filter and about 0.5% by the LOF outlier detection.

In v1.8, the quality filter is further improved using 18 million additional ocean scenes equally distributed over 30 days when training the random forest classifier. This reduces scenes with residual cloud cover especially concerning overcast conditions over the Arctic ocean in summer, which were not always reliably detected in previous product versions. The improvement is demonstrated by the example of July 2018 in Figure 5 showing the precision of the quality filter for retrievals classified as

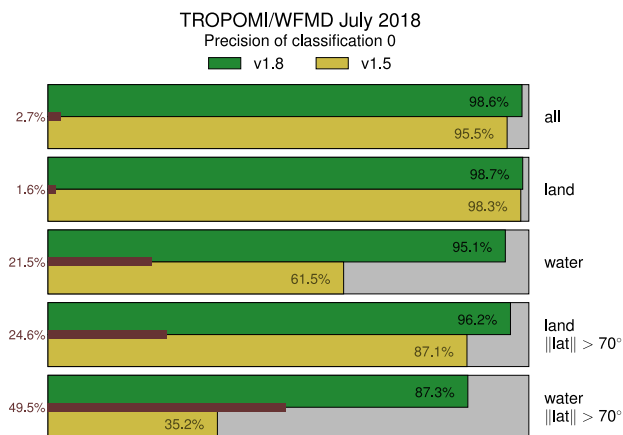


Figure 5. Percentage of actually cloud-free scenes according to VIIRS among all scenes passing the quality filter (precision of classification 0) for July 2018 shown in green and yellow for v1.8 and v1.5, respectively. The corresponding relative data loss of cloud-free scenes passing the quality filter due to the more stringent filtering in v1.8 compared to v1.5 is highlighted by the red bars.

good. The better the precision, the lower the false discovery rate of class 0, i.e. the fraction of scenes that are classified as good but should in fact be discarded according to VIIRS cloud information. Overall, the percentage of actually cloud-free scenes (defined via the condition that the fraction of VIIRS subscenes classified as *confidently cloudy* has to be smaller than < 0.1) in the quality filtered product is already very high in v1.5 ($> 95\%$). However, if restricted to the small subset of measurements at high latitudes over water, it turns out that a significant portion of measurements is misclassified. As this subset only accounts for about 1% of the total measurements, the eminent overall performance of the quality filter is not significantly affected. But for analyses that focus exclusively on high latitudes, the high false discovery rate for this small subgroup may adversely affect conclusive results, e.g. concerning Arctic methane trends. For this reason, the quality filter has been specifically made more stringent in v1.8 so that cloudiness is also detected with sufficient reliability for this challenging subgroup.

The implemented tightening of the quality filter not only increases the precision of class 0, it also decreases the associated recall, i.e. the percentage of all the cloud-free scenes that are correctly classified as good. The corresponding relative data loss is measured by the complement of the ratio of the respective recalls (v1.8 relative to v1.5) and is also shown in Figure 5. The largest loss of cloud-free data is observed for the Arctic Ocean (where the precision increase is also largest) with recall being about 50% lower for the updated v1.8 compared to v1.5. In this context, it is important to note that the computed relative data losses refer to cloud-free scenes and not to good measurements. Since not all cloud-free scenes necessarily result in good retrievals, the quality filter has also learned to additionally exclude retrievals with obvious methane biases (without using the primary retrieval parameters XCH_4 and XCO as features in the prediction of the quality) (Schneising et al., 2019), e.g. measurements with extremely low albedo such as ocean scenes beyond sun-glint or glitter. In this sense, the indicated unwanted relative data losses should rather be deemed to be an upper limit for the data losses of the actual good data as some scenes with adverse conditions may be properly removed even though they are cloud-free. In any case, the trade-off between

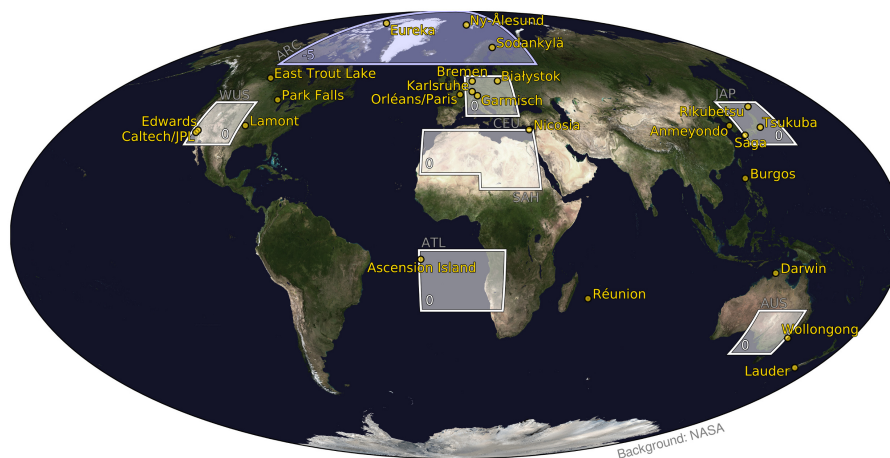


Figure 6. Illustration of the updated regions used in the training of the machine learning regressor, namely Arctic (ARC), Western United States (WUS), Central Europe (CEU), Japan (JAP), Sahara (SAH), South Atlantic (ATL), and Australia (AUS). Also given are the respective corrections in ppb for each region applied to the low-resolution methane climatology prior to learning. The yellow circles highlight sites of the TCCON used in the subsequent validation.

precision and recall is well justified because precision is much more important than recall in the presented setup. In other words, measurements predicted to be good that should actually be excluded are more critical than cloud-free scenes that are excluded. In the first case, likely biased retrievals are preserved, while in the second case potentially good data is lost, but data
230 quality is not negatively affected for the proportion that passes the filter.

3.3.2 Machine learning calibration for methane

Even after quality filtering some systematic errors may still be present in the remaining data due to approximations in the forward model or instrumental issues. As experience has shown, issues related to the surface reflectance and its spectral variability are of particular concern. Therefore, the fitted polynomial coefficient of degree zero p_0 is fed into the random forest regressor machine learning calibration as an additional feature since v1.5 to better account for potential spectral albedo variations.
235 This increases the number of features to 6, which are subsequently listed in order of importance: retrieved apparent albedo, across-track dimension index, solar zenith angle, polynomial coefficient p_0 , cloud parameter r_{cld} , and strong H_2O absorption radiance. Moreover, the training regions and calibration offsets are updated in accordance with Figure 6 to further improve global representativity, and the tree growing is extended to 5000 leaves. Up to and including v1.5, the training dataset was
240 limited to scenes with solar zenith angles smaller than 75° . In v1.8, the learning cut-off threshold is raised to 80° to get a better correction for high latitudes. Although demanding conditions with solar zenith angles of more than 75° are still excluded in the standard product as they may be subject to scattering and saturation related issues, this yields the possibility to analyse such scenes in an experimental setup if needed. Due to this learning augmentation, the tree growth was further increased to 10000 leaf nodes. However, compared to the total of about 70 million harvested scenes, the depth of the involved decision trees is still



245 considered shallow. It was explicitly confirmed by recursive feature elimination with cross-validation and reservation of 20%
 of the data for testing purposes that there is no overfitting linked to the number of features or the depth of the decision trees in
 the random forest.

The calibration is performed against the Simple cLimatological Model for atmospheric CH₄ (SLIMCH₄) v2021 in nearest
 neighbour mode without interpolation, whose validation with the Total Carbon Column Observing Network (TCCON) (Wunch
 250 et al., 2011) confirmed good quality and indicated that the greatest discrepancies occur in the Arctic (Noël et al., 2022). The
 biases at the Arctic sites are consistently positive ranging from about 12 ppb to 20 ppb. Therefore, the values of the climatology
 in the Arctic region are slightly modified by subtracting 5 ppb before learning to reduce the mean Arctic bias to a more typical
 level to further improve the validity of the low-resolution estimate of the true atmospheric state and thus allow the best possible
 identification and correction of the coarse-scale interrelationships with other parameters.

255 3.4 Wavelet decomposition and destriping

There is striping in flight direction in the TROPOMI XCH₄ and XCO data presumably due to different offsets and gains of
 pixels of the detector array used for the staring pushbroom concept (Borsdorff et al., 2019; Schneising et al., 2019). The vertical
 stripes in the satellite data are efficiently removed in v1.8 by combined wavelet-Fourier filtering while optimally preserving all
 other spatial information (Münch et al., 2009). The basic procedure for gapless data is described in the following subsection.

260 3.4.1 Basic procedure

First a 2D multilevel wavelet decomposition with symmetric boundary conditions is performed orbitwise separating horizontal,
 vertical, and diagonal details. More specifically, a wavelet decomposition of level L divides the 2D signal $f(x, y)$ into a low-
 frequency approximation (represented by a scaling function Φ_L and coefficients a_L), which still contains the self-similar
 complete signal information at lower resolution, and high-frequency detail bands (represented by wavelet functions Ψ_l and
 265 coefficients h_l, v_l, d_l for different scales $l \in \{1, \dots, L\}$). The set of coefficients representing the wavelet representation \mathcal{W} of
 $f(x, y)$ allows the lossless reconstruction of the original information:

$$f(x, y) = \sum_{m, n} a_{L, m, n} \Phi_{L, m, n}(x, y) + \sum_{b \in \{h, v, d\}} \sum_{l=1}^L \sum_{m, n} b_{l, m, n} \Psi_{b, l, m, n}(x, y) \quad (2)$$

$$f(x, y) \iff \mathcal{W} = \{a_L, h_l, v_l, d_l | l \in \{1, \dots, L\}\} \quad (3)$$

The 2D wavelet decomposition of an image with vertical stripes is demonstrated in Figure 7. The striping information is
 270 concentrated in the corresponding horizontal detail bands h_l .

In the following, only the fraction of the detail bands affected by stripes are Fourier-filtered while the other bands remain
 unchanged. Using fast Fourier transformation (FFT), the stripe information in the affected detail bands h_l is further condensed
 around $Y = 0$ in the frequency domain and attenuated by multiplication of the Fourier coefficients with a Gaussian function

$$g(X, Y) = 1 - \exp\left(\frac{-Y^2}{2\sigma^2}\right) \quad (4)$$

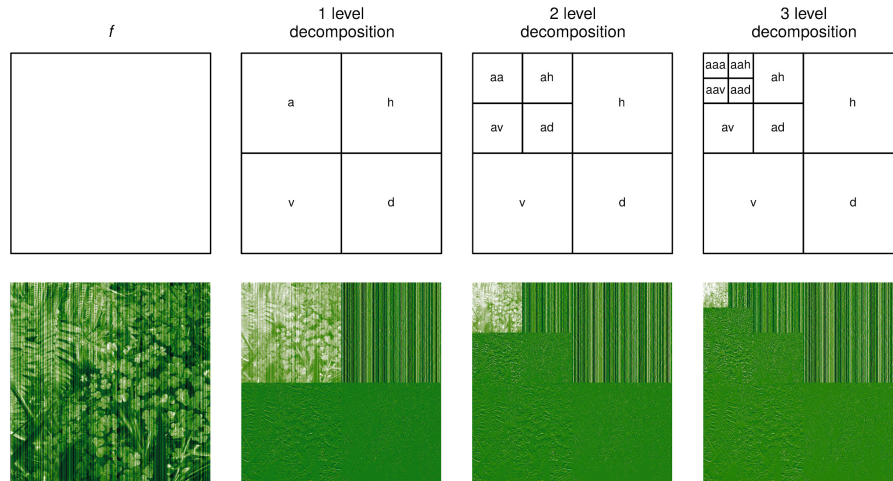


Figure 7. 2D wavelet decomposition of an image with vertical stripes for different decomposition levels. The low-pass approximation coefficients a_l still contain the self-similar complete signal information at a lower resolution; the other bands contain the details to reconstruct the higher resolution image. The striping information is concentrated to the detail bands represented by the coefficients h_l .

275 In the case of imperfect stripes with offset variability in stripe direction, the attenuation parameter σ has to be chosen larger than for ideal stripes to enable efficient destriping. However, σ should be as small as possible because original image information is also increasingly removed when σ becomes too large. The optimal choice of σ depends on the image and the characteristics of the striping artifacts.

Attenuation with $g(X, Y)$ and subsequent inverse FFT results in updated wavelet coefficients \tilde{h}_l . Reconstruction using these
 280 refined coefficients together with the original coefficients for the other bands results in the destriped signal $f_{\Psi, L}(x, y)$:

$$f_{\Psi, L}(x, y) \iff \tilde{\mathcal{W}} = \{a_L, \tilde{h}_l, v_l, d_l \mid l \in \{1, \dots, L\}\} \quad (5)$$

Combined wavelet-Fourier filtering has a better destriping performance than Fourier filtering alone because the majority of the coefficients remains entirely unchanged ensuring that the structural features outside the detail bands affected by stripes are preserved (Münch et al., 2009). The destriping performance is demonstrated in Figure 8.

285 3.4.2 Application to satellite data

Before the combined wavelet-Fourier destriping algorithm can be applied to satellite orbits $f(x, y)$, data missing from quality filtering must be filled in suitably. Initially, rows without data at all are filled with the median of f . For rows with data, the gaps in each row are filled with the row-wise median value and a stripe function $s_y(x)$ is determined by subtracting the median value from the original row y . A fitted cubic polynomial is also subtracted on the support of the original data to remove smooth
 290 horizontal gradients of s_y . Afterwards, the column-wise median of the previously calculated stripe functions is computed for all columns to add the median striping to the filled gaps. This results in $F(x, y)$ with completely filled domain and extended stripes



Figure 8. Performance of the combined wavelet-Fourier filter using Coiflet wavelets (coif16), $\sigma = 2$, and different decomposition levels L .

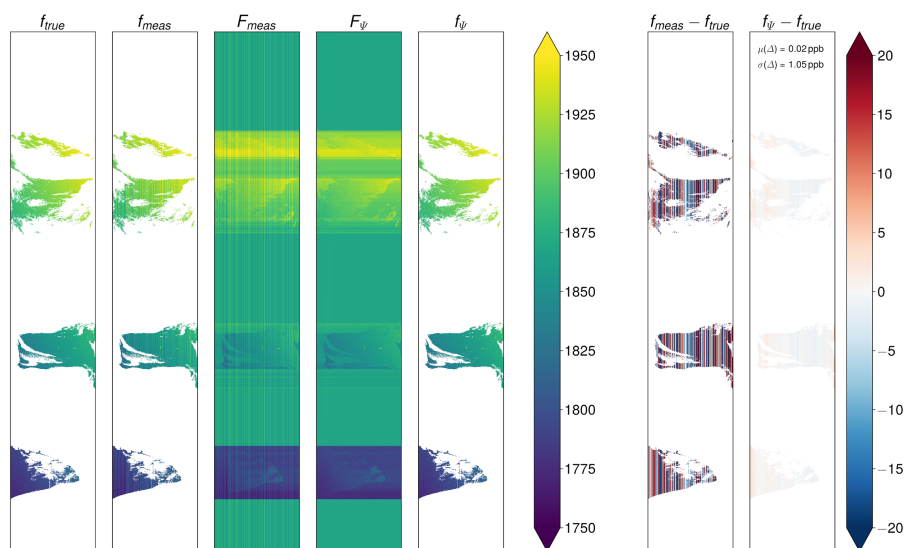


Figure 9. Illustration of the performance of combined wavelet-Fourier filtering for a synthetic orbit with significant gaps using Coiflets (coif16), $\sigma = 2$, and $L = 7$. Thereby, f_{true} is the true distribution, f_{meas} is the distribution as measured by the instrument (with stripes), F_{meas} is the distribution after filling, F_{Ψ} is the filter result of F_{meas} , and f_{Ψ} is the final destriped result after restriction to the original support. The other two columns show the respective differences of the measured and destriped distribution to the truth.

in vertical direction meeting the requirements for wavelet-Fourier filtering. After destriping of F , the function is restricted to the original support. The whole procedure

$$f \longrightarrow F \longrightarrow F_{\Psi} \longrightarrow f_{\Psi} = F_{\Psi}|_{\text{supp}(f)} \quad (6)$$

295 is illustrated in Figure 9 demonstrating that the original true distribution is very well reconstructed by the destriping algorithm. In the case of the TROPOMI/WFMD products, Coiflets of order 16 (coif16), $\sigma = 2$, and $L = 7$ proved to be suitable choices for the wavelet family, the attenuation parameter, and the wavelet decomposition level.

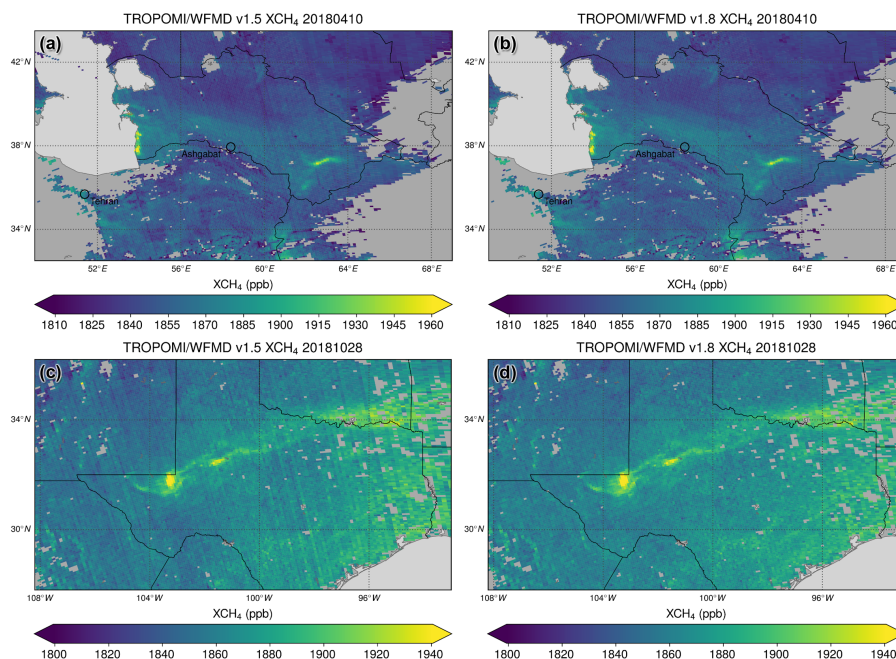


Figure 10. Performance of the destriping filter for two example scenes in Turkmenistan (a,b) and the United States (c,d) with XCH₄ enhancements due to emissions from the oil and gas industry. Panels (a) and (c) show the previous version, panels (b) and (d) the improved version with destriping.

The performance of the destriping filter is shown in Figure 10 for genuine TROPOMI data using two example scenes in Turkmenistan and the United States known for large methane emissions from the oil and gas industry. Just as in Figure 2 for the Etosha pan, it is immediately apparent that the striping decreases significantly in the latest product version.

4 Overview of the products

The improved XCH₄ and XCO products currently cover a period of 4.5 years, starting at mission launch in autumn 2017 up to and including April 2022, and will be regularly updated. Global yearly distributions from 2018 to 2021 of both products are shown in Figures 11 and 12, respectively. As can be seen, the quality filtered datasets have similar coverage from year to year including high latitudes and the oceans. For both gases the interhemispheric gradient and increments over major source regions, such as those related to anthropogenic emissions in China, India, and Southeast Asia, are clearly detected. In the XCO case, source regions associated with biomass burning (tropical Africa and South America) and wildfires (Canada and Siberia) are also visible. While there is an accelerating growth of atmospheric methane for the considered time period, the annual mean increase of XCO is decelerating with almost stable mean values in 2020 and 2021, which are slightly larger than in the two previous years, presumably due to stronger wildfire activity in the boreal zone.

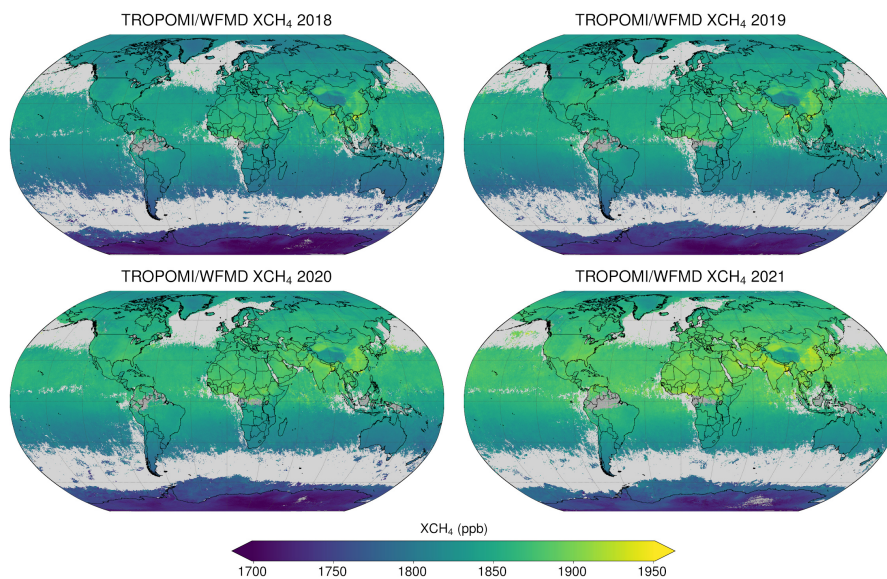


Figure 11. Yearly averages of TROPOMI/WFMD v1.8 XCH₄ shown on a $0.1^\circ \times 0.1^\circ$ grid.

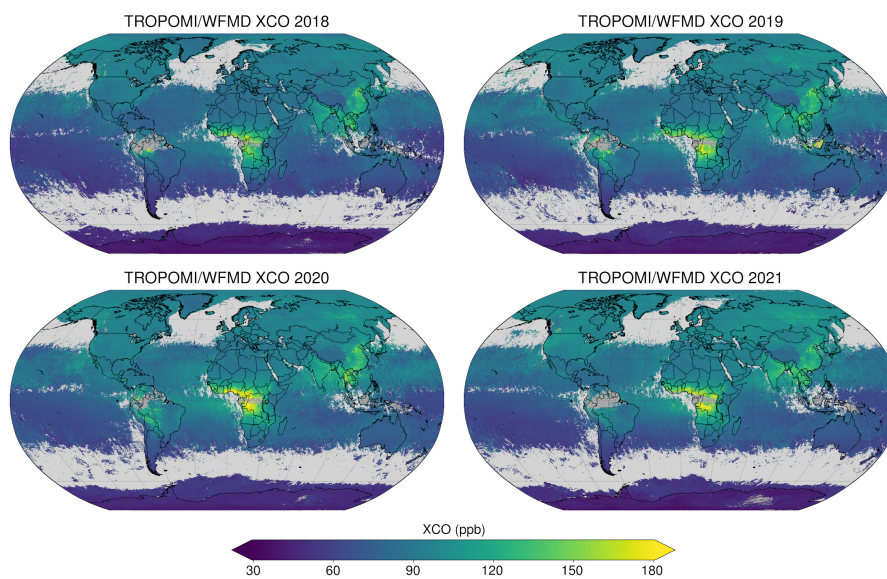


Figure 12. As Figure 11 but for TROPOMI/WFMD v1.8 XCO.



To further investigate the annual increase of the products, time series of globally-averaged monthly gridded data ($0.1^\circ \times 0.1^\circ$, weighted by area) are decomposed into a seasonal and a trend component using Locally Estimated Scatterplot Smoothing (LOESS) (Cleveland et al., 1990). LOESS smoothes a function of variables by local polynomial regression using a smoothing kernel based on the tricube weight function with compact support. The kernel width can be adjusted separately for the different components by specifying related smoothing parameters. To get a decomposition that is robust to outliers, two recursive procedures are performed: an inner loop updating the seasonal and trend components nested inside an outer loop computing robustness weights to be used in the next run of the inner loop. The Seasonal and Trend decomposition using LOESS (STL) has several advantages over simpler deseasonalisation methods such as subtracting a 12-month running mean: 1) the trend is computed for the entire data record including both ends of the time series, 2) the smoothness of the components can be controlled by the user, 3) the component estimates are not affected by occasional outliers in the robust estimation. STL has 6 different parameters to specify: the periodicity of the sequence n_p , the smoothing parameters n_l , n_t , n_s for low-pass filter, trend, and seasonal component, as well as the number of passes through the inner and the outer loop, n_i and n_o . There is also a generalisation called MSTL to support multiple seasonalities by applying the STL procedure iteratively to seamlessly separate the different seasonal cycles (Bandara et al., 2021).

We follow the original implementation of Cleveland et al. (1990) using $n_i = 5$ and $n_o = 0$ as the robust estimation of seasonal and trend components is not needed, $n_p = 12$ for monthly data, $n_l = \lceil n_p \rceil_{\text{odd}} = 13$, and $n_t = \lceil 1.5 \cdot n_p / (1 - 1.5/n_s) \rceil_{\text{odd}}$. According to this settings the only free parameter is n_s , which then also determines n_t by the formula given above. We choose $n_s = 27$ as compromise between the mutually dependent smoothnesses of the seasonal and the trend component. We restrict this analysis to data since April 2018, because the data density during the previous commissioning phase of TROPOMI is significantly reduced. Empirical results from both marine surface and TROPOMI satellite data have shown that the residual component decreases significantly when adding an extra seasonality $n_{\tilde{p}} = 9$ to the decomposition. Therefore, we perform a corresponding MSTL with 100 iterations to separate the two seasonalities n_p and $n_{\tilde{p}}$. After decomposition, the annual increase in a given year is defined as the increase in the abundance of the trend component from the January mean value in that year to the January mean value of the next year. The monthly means and the components are shown in Figure 13.

As TROPOMI is a passive spectrometer, the latitudinal coverage of quality filtered data differs with season as a consequence of the different illumination conditions, e.g. there is no good data at high latitudes during polar night. Although these regional seasonal gaps may limit the independent trend analysis for small latitude bands in polar regions, the presented analysis of annual increases based on globally-averaged monthly data is not severely affected because there are no gaps in the global time series and the seasonal sampling of the temporally consistent TROPOMI/WFMD products is similar from year to year. The impact of the choice of the seasonal smoothing parameter n_s , the extra seasonality $n_{\tilde{p}}$, and the different seasonal sampling is taken into account in the uncertainty analysis.

The resulting annual increases corroborate the accelerated growth of $X\text{CH}_4$ (2019: 7.9 ppb, 2020: 15.0 ppb, 2021: 17.5 ppb) and the decelerated growth of $X\text{CO}$ (2019: 4.5 ppb, 2020: 0.1 ppb, 2021: 1.2 ppb) during the covered period already indicated in the annual averages of Figures 11 and 12. The uncertainties of the annual increases are estimated by two times the root sum square of four components: the standard deviation of a set of increases induced by 1) bootstrap resampling of the

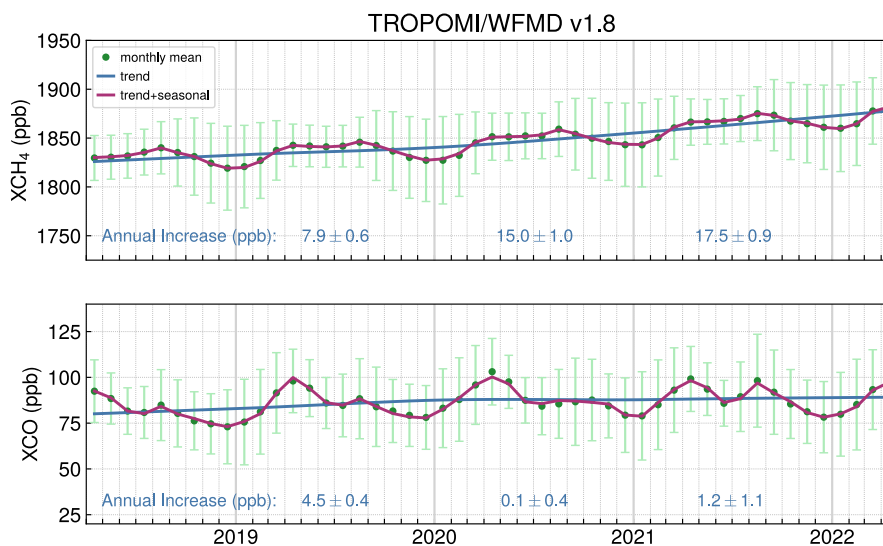


Figure 13. Time series of globally-averaged monthly gridded TROPOMI/WFMD v1.8 data. The underlying area-weighted monthly means are shown as green dots with the associated standard deviation as bars in lighter green. The season-trend decomposition used to derive the annual increase is done using Locally Estimated Scatterplot Smoothing (LOESS). The trend component is shown in blue and the sum of trend and seasonal component is shown in purple.

global gridboxes contributing to the monthly means, 2) randomly modifying the data to take the uncertainties of the retrieved column-averaged mole fractions into account, 3) randomly modifying the seasonal smoothing parameter n_s as well as randomly including or excluding high latitudes ($|\text{lat}| > 70^\circ$) and the additional seasonality $n_{\bar{p}}$ independently of each other, and 4) randomly shifting the timeseries by 0 or ± 1 time steps. The corresponding sample size in the estimation of all uncertainty components is 5000, i.e. 5000 alternative increases are calculated per year and component to be included in the analysis.

As can be seen from the comparison in Figure 14, the derived temporal development of the annual global methane increases is consistent with the trends determined from marine surface sites of the Global Monitoring Division of NOAA's Earth System Research Laboratory (Dlugokencky, 2022) with two consecutive annual record growth rates in 2020 and 2021.

To compare the performance of the different TROPOMI/WFMD versions, the products are validated with the ground-based Total Carbon Column Observing Network (TCCON) (Wunch et al., 2011), which uses similar Fourier Transform Spectrometer (FTS) instrumentation and a common retrieval algorithm network-wide. Table 1 compares the most important figures of merit obtained by validation with the GGG2014 version of TCCON data at 26 sites (see Table A1) using the well-established validation procedure described in detail in Schneising et al. (2019). We use the TCCON GGG2014 version instead of the newer GGG2020 product, because not all sites have been reprocessed at time of submission. The analysis of regional biases based on GGG2014 is therefore more robust due to the larger number of regions covered.

To ensure comparability of the results for the different versions, the comparison was restricted consistently to a match period ending 2020. Since the derived systematic errors of the satellite products are comparable in magnitude to the station-

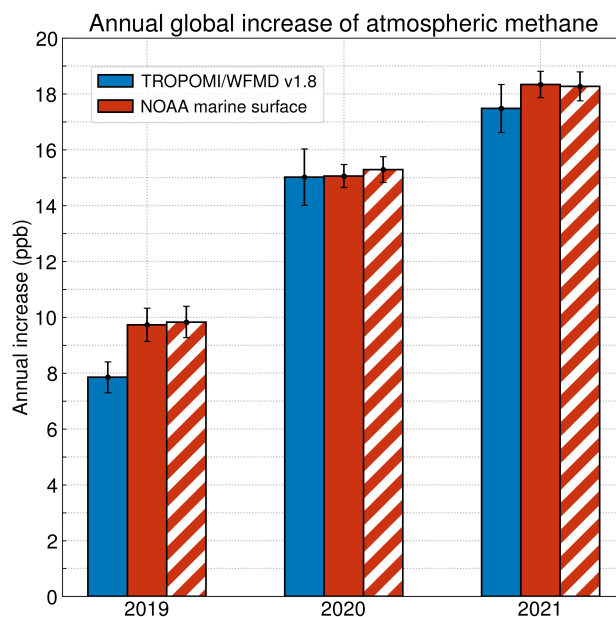


Figure 14. Comparison of the annual global increases of TROPOMI/WFMD v1.8 XCH₄ (blue) and NOAA marine surface CH₄ (red) as reported by Dlugokencky (2022). The hatched red bar is a consistency check illustrating the results when using the method presented here to determine the increases on the monthly means provided by NOAA (Dlugokencky, 2022).

Table 1. Comparisons of the most important figures of merit for the different TROPOMI/WFMD product versions obtained by validation with the GGG2014 version of TCCON data at 26 sites (see Table A1). The random error is measured by the scatter of the satellite data relative to the TCCON, the systematic error is a combination of the spatial station-to-station bias and the seasonal bias. *N* is the total number of collocations for all sites together.

Data product	Random error (ppb)			Systematic error (ppb)			<i>N</i>		
	v1.2	v1.5	v1.8	v1.2	v1.5	v1.8	v1.2	v1.5	v1.8
Methane (XCH ₄)	14.2	12.8	12.4	5.0	5.1	5.2	615435	649041	614469
Carbon monoxide (XCO)	5.3	5.3	5.1	2.4	2.3	2.6			

to-station 1σ -accuracy of the TCCON, estimated to be 2 ppb for XCO and 3.5 ppb for XCH₄ (Wunch et al., 2010), all TROPOMI/WFMD products are equivalent in terms of systematic error, although there are small deviations (in the range of tenths of ppb) for the different versions. Since the precision of TCCON is appreciably better compared to the satellite data, the improvement in the random error is considered significant, in particular in the case of methane, and is ascribed to the reduction of the pseudo-noise component due to the algorithm improvements, e.g. the efficient destriping algorithm and the optimised quality filter reducing the number of outliers.



5 Conclusions

370 We have introduced the changes implemented in the latest version v1.8 of the combined scientific TROPOMI/WFMD XCH₄
and XCO product, which currently covers 4.5 years of data from mission start until end of April 2022 and will be further
extended in the future. It was demonstrated that the performance of the updated retrieval algorithm was further improved,
for example with respect to striping in flight direction for single overpasses due to a dedicated destriping algorithm, which
simultaneously preserves the actual spatial trace gas features. Together with the other advancements, such as an optimised
375 quality filter reducing the number of outliers and the usage of an improved Digital Elevation Model, this reduces the pseudo-
noise component resulting in an improved random error estimated by validation with the Total Carbon Column Observing
Network.

Due to the machine learning-based quality filter, current cloud information is no longer required after the initial supervised
learning process is completed. As a consequence, the algorithm is independent of the availability or consistency of cloud
380 products, such as VIIRS, as the algorithm has learned to classify good quality measurements entirely by intrinsic parameters
available from or used in the preceding processing excluding the primary retrieval parameters XCH₄ and XCO. The resulting
consistent data products with similar spatial coverage from year to year are not only generally useful for detecting and quanti-
fying emission sources, but also enable long-term applications such as trend determination. In the case of methane, the derived
global annual increases are consistent with the trends determined from marine surface sites of the Global Monitoring Division
385 of NOAA's Earth System Research Laboratory exhibiting an accelerated growth for the period covered by the TROPOMI data
with two consecutive annual record growth rates in 2020 and 2021.

Although the natural and anthropogenic source and sink processes for CH₄ and CO are known, it is still a challenge to
identify the exact contributions of the different processes to the observed annual growth rate variations. Especially for methane
this lack of detailed understanding is critical as it complicates climate projections and the specification of effective emission
390 mitigation strategies. A better estimate of the source and sink budget can be inferred by exploiting a comprehensive monitoring
system, which compiles complementary information from accurate local in situ measurements and satellite observations of
ample coverage, within an inverse modelling framework. High quality TROPOMI products with their unique combination of
high precision, spatiotemporal resolution, and global coverage offer a valuable opportunity in this context.



Appendix A: List of TCCON sites

Table A1. TCCON sites used in the validation sorted by latitude from north to south.

Station	Latitude (°)	Longitude (°)	Altitude (km)	Reference
Eureka	80.05	−86.42	0.61	Strong et al. (2019)
Ny-Ålesund	78.92	11.92	0.02	Notholt et al. (2017)
Sodankylä	67.37	26.63	0.19	Kivi et al. (2014)
East Trout Lake	54.35	−104.99	0.50	Wunch et al. (2018)
Białystok	53.23	23.03	0.19	Deutscher et al. (2015)
Bremen	53.10	8.85	0.03	Notholt et al. (2014)
Karlsruhe	49.10	8.44	0.11	Hase et al. (2015)
Paris	48.85	2.36	0.06	Te et al. (2014)
Orléans	47.97	2.11	0.13	Warneke et al. (2014)
Garmisch	47.48	11.06	0.75	Sussmann and Rettinger (2018)
Park Falls	45.94	−90.27	0.44	Wennberg et al. (2017)
Rikubetsu	43.46	143.77	0.38	Morino et al. (2018c)
Lamont	36.60	−97.49	0.32	Wennberg et al. (2016b)
Anmeyondo	36.54	126.33	0.03	Goo et al. (2014)
Tsukuba	36.05	140.12	0.03	Morino et al. (2018a)
Nicosia	35.14	33.38	0.19	Petri et al. (2020)
Edwards	34.96	−117.88	0.70	Iraci et al. (2016)
JPL	34.20	−118.18	0.39	Wennberg et al. (2016a)
Caltech	34.14	−118.13	0.24	Wennberg et al. (2015)
Saga	33.24	130.29	0.01	Shiomi et al. (2014)
Burgos	18.53	120.65	0.04	Morino et al. (2018b)
Ascension Island	−7.92	−14.33	0.03	Feist et al. (2014)
Darwin	−12.46	130.93	0.04	Griffith et al. (2014a)
Réunion	−20.90	55.49	0.09	De Mazière et al. (2017)
Wollongong	−34.41	150.88	0.03	Griffith et al. (2014b)
Lauder	−45.04	169.68	0.37	Sherlock et al. (2014)



395 *Data availability.* The methane and carbon monoxide data products presented in this publication are available at http://www.iup.uni-bremen.de/carbon_ghg/products/tropomi_wfmd/.

Author contributions. OS designed and operated the TROPOMI/WFMD satellite retrievals, performed the data analysis, interpreted the results, and wrote the paper. MiB, JH, SV, MR, MaB, HB, and JPB provided significant conceptual input to the design of the retrievals and the improvement of the paper. All authors discussed the results and commented on the paper.

400 *Competing interests.* The authors declare that they have no conflict of interest.

Acknowledgements. This publication contains modified Copernicus Sentinel data (2018-2022). Sentinel-5 Precursor is an ESA mission implemented on behalf of the European Commission. The TROPOMI payload is a joint development by ESA and the Netherlands Space Office (NSO). The Sentinel-5 Precursor ground-segment development has been funded by ESA and with national contributions from The Netherlands, Germany, and Belgium.

405 We acknowledge the use of VIIRS imagery from the NASA Worldview application (<https://worldview.earthdata.nasa.gov/>) operated by the NASA/Goddard Space Flight Center Earth Science Data and Information System (ESDIS) project and thank the European Centre for Medium-Range Weather Forecasts (ECMWF) for providing the ERA5 reanalysis. TCCON data were obtained from the TCCON Data Archive, hosted by CaltechDATA, California Institute of Technology (<https://tccodata.org/>); we thank the TCCON partners for their efforts to operate the TCCON sites, which are an essential validation resource for satellite products.

410 *Financial support.* The research leading to the presented results received funding from the European Space Agency (ESA) via the projects GHG-CCI+ and MethaneCAMP (ESA contract nos. 4000126450/19/I-NB and 4000137895/22/I-AG). The TROPOMI/WFMD retrievals presented here were performed on HPC facilities of the IUP, University of Bremen, funded under DFG/FUGG grant nos. INST 144/379-1 and INST 144/493-1. The research received additional funding from the University of Bremen as part of the junior research group “Greenhouse gases in the Arctic” and from the Deutsche Forschungsgemeinschaft (DFG project no. 268020496 - TRR 172) within the Transregional
415 Collaborative Research Center “Arctic Amplification: Climate Relevant Atmospheric and Surface Processes, and Feedback Mechanisms (AC)³”. The article processing charges for this open-access publication were covered by the University of Bremen.



References

- Airbus: Copernicus Global Digital Elevation Model - Validation Report, https://spacedata.copernicus.eu/documents/20126/0/GEO1988-CopernicusDEM-RP-001_ValidationReport_V1.0.pdf, 2020.
- 420 Bandara, K., Hyndman, R. J., and Bergmeir, C.: MSTL: A Seasonal-Trend Decomposition Algorithm for Time Series with Multiple Seasonal Patterns, arXiv:2107.13462, <https://doi.org/10.48550/arXiv.2107.13462>, 2021.
- Beugler-Bell, H. and Buch, M. W.: Soils and soil erosion in the Etosha National Park, northern Namibia, *Madoqua*, 20, 91–104, https://hdl.handle.net/10520/AJA10115498_460, 1997.
- Borsdorff, T., van de Brugh, J., Schneider, A., Lorente, A., Birk, M., Wagner, G., Kivi, R., Hase, F., Feist, D. G., Sussmann, R., Rettinger, M.,
425 Wunch, D., Warneke, T., and Landgraf, J.: Improving the TROPOMI CO data product: update of the spectroscopic database and destriping of single orbits, *Atmos. Meas. Tech.*, 12, 5443–5455, <https://doi.org/10.5194/amt-12-5443-2019>, 2019.
- Bovensmann, H., Burrows, J. P., Buchwitz, M., Frerick, J., Noël, S., Rozanov, V. V., Chance, K. V., and Goede, A. P. H.: SCIAMACHY – Mission Objectives and Measurement Modes, *J. Atmos. Sci.*, 56, 127–150, [https://doi.org/10.1175/1520-0469\(1999\)056<0127:SMOAMM>2.0.CO;2](https://doi.org/10.1175/1520-0469(1999)056<0127:SMOAMM>2.0.CO;2), 1999.
- 430 Breunig, M. M., Kriegel, H.-P., Ng, R. T., and Sander, J.: LOF: Identifying Density-Based Local Outliers, *ACM SIGMOD Rec.*, 29, 93–104, <https://doi.org/10.1145/335191.335388>, 2000.
- Buchwitz, M., de Beek, R., Burrows, J. P., Bovensmann, H., Warneke, T., Notholt, J., Meirink, J. F., Goede, A. P. H., Bergamaschi, P., Körner, S., Heimann, M., and Schulz, A.: Atmospheric methane and carbon dioxide from SCIAMACHY satellite data: initial comparison with chemistry and transport models, *Atmos. Chem. Phys.*, 5, 941–962, <https://doi.org/10.5194/acp-5-941-2005>, 2005.
- 435 Buchwitz, M., Khlystova, I., Bovensmann, H., and Burrows, J. P.: Three years of global carbon monoxide from SCIAMACHY: comparison with MOPITT and first results related to the detection of enhanced CO over cities, *Atmos. Chem. Phys.*, 7, 2399–2411, <https://doi.org/10.5194/acp-7-2399-2007>, 2007.
- Buchwitz, M., Schneising, O., Reuter, M., Heymann, J., Krautwurst, S., Bovensmann, H., Burrows, J. P., Boesch, H., Parker, R. J., Somkuti, P., Detmers, R. G., Hasekamp, O. P., Aben, I., Butz, A., Frankenberg, C., and Turner, A. J.: Satellite-derived methane hotspot emission
440 estimates using a fast data-driven method, *Atmos. Chem. Phys.*, 17, 5751–5774, <https://doi.org/10.5194/acp-17-5751-2017>, 2017.
- Burrows, J. P., Hölzle, E., Goede, A. P. H., Visser, H., and Fricke, W.: SCIAMACHY – Scanning Imaging Absorption Spectrometer for Atmospheric Chartography, *Acta Astronautica*, 35, 445–451, [https://doi.org/10.1016/0094-5765\(94\)00278-T](https://doi.org/10.1016/0094-5765(94)00278-T), 1995.
- Cleveland, R. B., Cleveland, W. S., McRae, J. E., and Terpenning, I.: STL: A Seasonal-Trend Decomposition Procedure Based on Loess, *Journal of Official Statistics*, 6, 3–73, 1990.
- 445 Cusworth, D. H., Duren, R. M., Thorpe, A. K., Pandey, S., Maasackers, J. D., Aben, I., Jervis, D., Varon, D. J., Jacob, D. J., Randles, C. A., Gautam, R., Omara, M., Schade, G. W., Dennison, P. E., Frankenberg, C., Gordon, D., Lopinto, E., and Miller, C. E.: Multi-satellite Imaging of a Gas Well Blowout Enables Quantification of Total Methane Emissions, *Geophys. Res. Lett.*, 48, e2020GL090864, <https://doi.org/https://doi.org/10.1029/2020GL090864>, 2021.
- De Mazière, M., Sha, M. K., Desmet, F., Hermans, C., Scolas, F., Kumps, N., Metzger, J.-M., Dufлот, V., and Cammas, J.-P.: TCCON data
450 from Réunion Island (La Réunion), France, Release GGG2014.R1. TCCON data archive, hosted by CaltechDATA, California Institute of Technology, <https://doi.org/10.14291/tccon.ggg2014.reunion01.r1>, 2017.



- Deutscher, N. M., Notholt, J., Messerschmidt, J., Weinzierl, C., Warneke, T., Petri, C., and Grupe, P.: TCCON data from Bialystok, Poland, Release GGG2014.R1. TCCON data archive, hosted by CaltechDATA, California Institute of Technology, <https://doi.org/10.14291/tcon.ggg2014.bialystok01.r1/1183984>, 2015.
- 455 Dlugokencky, E. J.: Annual Increase in Globally-Averaged Atmospheric Methane, NOAA/GML, (last access: 7 September 2022), https://gml.noaa.gov/ccgg/trends_ch4/, 2022.
- Drummond, J. R., Zou, J., Nichitiu, F., Kar, J., Deschambaut, R., and Hackett, J.: A review of 9-year performance and operation of the MOPITT instrument, *Adv. Space Res.*, 45, 760–774, <https://doi.org/10.1016/j.asr.2009.11.019>, 2010.
- European Space Agency, S.: Copernicus Global Digital Elevation Model. Distributed by OpenTopography, <https://doi.org/10.5069/G9028PQB>, 2021.
- 460 Feist, D. G., Arnold, S. G., John, N., and Geibel, M. C.: TCCON data from Ascension Island, Saint Helena, Ascension and Tristan da Cunha, Release GGG2014.R0. TCCON data archive, hosted by CaltechDATA, California Institute of Technology, <https://doi.org/10.14291/tcon.ggg2014.ascension01.r0/1149285>, 2014.
- Fowler, D., Amann, M., Anderson, R., Ashmore, M., Cox, P., Depledge, M., Derwent, D., Grennfelt, P., Hewitt, N., Hov, O., Jenkin, M., 465 Kelly, F., Liss, P., Pilling, M., Pyle, J., Slingo, J., and Stevenson, D.: Ground-level ozone in the 21st century: Future trends, impacts and policy implications, Royal Society Science Policy Report 15/08, available at: https://royalsociety.org/~media/Royal_Society_Content/policy/publications/2008/7925.pdf, 2008.
- Frankenberg, C., Meirink, J. F., Bergamaschi, P., Goede, A. P. H., Heimann, M., Körner, S., Platt, U., van Weele, M., and Wagner, T.: Satellite chartography of atmospheric methane from SCIAMACHY onboard ENVISAT: Analysis of the years 2003 and 2004, *J. Geophys. Res.*, 470 111, D07303, <https://doi.org/10.1029/2005JD006235>, 2006.
- Goo, T.-Y., Oh, Y.-S., and Velasco, V. A.: TCCON data from Anmyeondo, South Korea, Release GGG2014.R0. TCCON data archive, hosted by CaltechDATA, California Institute of Technology, <https://doi.org/10.14291/tcon.ggg2014.anmeyondo01.r0/1149284>, 2014.
- Griffith, D. W., Deutscher, N. M., Velasco, V. A., Wennberg, P. O., Yavin, Y., Keppel-Aleks, G., Washenfelder, R. A., Toon, G. C., Blavier, J.-F., Paton-Walsh, C., Jones, N. B., Kettlewell, G. C., Connor, B. J., Macatangay, R. C., Roehl, C., Ryzek, M., Glowacki, J., Culgan, T., and 475 Bryant, G. W.: TCCON data from Darwin, Australia, Release GGG2014.R0. TCCON data archive, hosted by CaltechDATA, California Institute of Technology, <https://doi.org/10.14291/tcon.ggg2014.darwin01.r0/1149290>, 2014a.
- Griffith, D. W., Velasco, V. A., Deutscher, N. M., Paton-Walsh, C., Jones, N. B., Wilson, S. R., Macatangay, R. C., Kettlewell, G. C., Buchholz, R. R., and Riggenbach, M. O.: TCCON data from Wollongong, Australia, Release GGG2014.R0. TCCON data archive, hosted by CaltechDATA, California Institute of Technology, <https://doi.org/10.14291/tcon.ggg2014.wollongong01.r0/1149291>, 2014b.
- 480 Hachmeister, J., Schneising, O., Buchwitz, M., Lorente, A., Borsdorff, T., Burrows, J. P., Notholt, J., and Buschmann, M.: On the influence of underlying elevation data on Sentinel-5 Precursor TROPOMI satellite methane retrievals over Greenland, *Atmos. Meas. Tech.*, 15, 4063–4074, <https://doi.org/10.5194/amt-15-4063-2022>, 2022.
- Hase, F., Blumenstock, T., Dohe, S., Groß, J., and Kiel, M.: TCCON data from Karlsruhe, Germany, Release GGG2014.R1. TCCON data archive, hosted by CaltechDATA, California Institute of Technology, <https://doi.org/10.14291/tcon.ggg2014.karlsruhe01.r1/1182416>, 485 2015.
- Hersbach, H., Bell, B., Berrisford, P., Hirahara, S., Horányi, A., Muñoz-Sabater, J., Nicolas, J., Peubey, C., Radu, R., Schepers, D., Simmons, A., Soci, C., Abdalla, S., Abellan, X., Balsamo, G., Bechtold, P., Biavati, G., Bidlot, J., Bonavita, M., De Chiara, G., Dahlgren, P., Dee, D., Diamantakis, M., Dragani, R., Flemming, J., Forbes, R., Fuentes, M., Geer, A., Haimberger, L., Healy, S., Hogan, R. J., Hólm, E., Janisková, M., Keeley, S., Laloyaux, P., Lopez, P., Lupu, C., Radnoti, G., de Rosnay, P., Rozum, I., Vamborg, F., Vil-



- 490 laume, S., and Thépaut, J.-N.: The ERA5 global reanalysis, *Quarterly Journal of the Royal Meteorological Society*, 146, 1999–2049,
<https://doi.org/https://doi.org/10.1002/qj.3803>, 2020.
- Hu, H., Hasekamp, O., Butz, A., Galli, A., Landgraf, J., Aan de Brugh, J., Borsdorff, T., Scheepmaker, R., and Aben, I.: The operational
methane retrieval algorithm for TROPOMI, *Atmos. Meas. Tech.*, 9, 5423–5440, <https://doi.org/10.5194/amt-9-5423-2016>, 2016.
- Hutchison, K. D. and Cracknell, A. P.: *Visible Infrared Imager Radiometer Suite: A New Operational Cloud Imager*, CRC Press of Taylor
495 and Francis, London, 2005.
- Iraci, L. T., Podolske, J. R., Hillyard, P. W., Roehl, C., Wennberg, P. O., Blavier, J.-F., Landeros, J., Allen, N., Wunch, D.,
Zavaleta, J., Quigley, E., Osterman, G. B., Albertson, R., Dunwoody, K., and Boyden, H.: TCCON data from Edwards,
California, USA, Release GGG2014.R1. TCCON data archive, hosted by CaltechDATA, California Institute of Technology,
<https://doi.org/10.14291/tcon.ggg2014.edwards01.r1/1255068>, 2016.
- 500 Kivi, R., Heikkinen, P., and Kyrö, E.: TCCON data from Sodankylä, Finland, Release GGG2014.R0. TCCON data archive, hosted by
CaltechDATA, California Institute of Technology, <https://doi.org/10.14291/tcon.ggg2014.sodankyla01.r0/1149280>, 2014.
- Kuze, A., Suto, H., Shiomi, K., Kawakami, S., Tanaka, M., Ueda, Y., Deguchi, A., Yoshida, J., Yamamoto, Y., Kataoka, F., Taylor, T. E.,
and Buijs, H. L.: Update on GOSAT TANSO-FTS performance, operations, and data products after more than 6 years in space, *At-
mos. Meas. Tech.*, 9, 2445–2461, <https://doi.org/10.5194/amt-9-2445-2016>, 2016.
- 505 Landgraf, J., aan de Brugh, J., Scheepmaker, R., Borsdorff, T., Hu, H., Houweling, S., Butz, A., Aben, I., and Hasekamp, O.:
Carbon monoxide total column retrievals from TROPOMI shortwave infrared measurements, *Atmos. Meas. Tech.*, 9, 4955–4975,
<https://doi.org/10.5194/amt-9-4955-2016>, 2016.
- Lorente, A., Borsdorff, T., Butz, A., Hasekamp, O., aan de Brugh, J., Schneider, A., Wu, L., Hase, F., Kivi, R., Wunch, D., Pollard, D. F.,
Shiomi, K., Deutscher, N. M., Velazco, V. A., Roehl, C. M., Wennberg, P. O., Warneke, T., and Landgraf, J.: Methane retrieved from
510 TROPOMI: improvement of the data product and validation of the first 2 years of measurements, *Atmos. Meas. Tech.*, 14, 665–684,
<https://doi.org/10.5194/amt-14-665-2021>, 2021.
- Masson-Delmotte, V., Zhai, P., Pirani, A., Connors, S. L., Péan, C., Berger, S., Caud, N., Chen, Y., Goldfarb, L., Gomis, M. I., Huang, M.,
Leitzell, K., Lonnoy, E., Matthews, J. B. R., Maycock, T. K., Waterfield, T., Yelekci, O., Yu, R., and Zhou, B., eds.: *Climate Change 2021:
The physical science basis. Contribution of Working Group I to the Sixth Assessment Report of the Intergovernmental Panel on Climate
515 Change (IPCC)*, Cambridge University Press, <https://doi.org/10.1017/9781009157896>, 2021.
- Moreira, L. C. J., Dos Santos Teixeira, A., and Galvao, L. S.: Laboratory Salinization of Brazilian Alluvial Soils and the Spectral Effects of
Gypsum, *Remote Sensing*, 6, 2647–2663, <https://doi.org/10.3390/rs6042647>, 2014.
- Morino, I., Matsuzaki, T., and Horikawa, M.: TCCON data from Tsukuba, Ibaraki, Japan, 125HR, Release GGG2014.R2. TCCON data
archive, hosted by CaltechDATA, California Institute of Technology, <https://doi.org/10.14291/tcon.ggg2014.tsukuba02.r2>, 2018a.
- 520 Morino, I., Velazco, V. A., Hori, A., Uchino, O., and Griffith, D. W. T.: TCCON data from Burgos, Philippines, Release GGG2014.R0.
TCCON data archive, hosted by CaltechDATA, California Institute of Technology, <https://doi.org/10.14291/tcon.ggg2014.burgos01.r0>,
2018b.
- Morino, I., Yokozeki, N., Matsuzaki, T., and Horikawa, M.: TCCON data from Rikubetsu, Hokkaido, Japan, Release GGG2014.R2. TCCON
data archive, hosted by CaltechDATA, California Institute of Technology, <https://doi.org/10.14291/tcon.ggg2014.rikubetsu01.r2>, 2018c.
- 525 Münch, B., Trtik, P., Marone, F., and Stampanoni, M.: Stripe and ring artifact removal with combined wavelet – Fourier filtering, *Optics
Express*, 17, 8567–8591, <https://doi.org/10.1364/OE.17.008567>, 2009.



- Noël, S., Reuter, M., Buchwitz, M., Borchardt, J., Hilker, M., Schneising, O., Bovensmann, H., Burrows, J. P., Di Noia, A., Parker, R. J., Suto, H., Yoshida, Y., Buschmann, M., Deutscher, N. M., Feist, D. G., Griffith, D. W. T., Hase, F., Kivi, R., Liu, C., Morino, I., Notholt, J., Oh, Y.-S., Ohyama, H., Petri, C., Pollard, D. F., Rettinger, M., Roehl, C., Rousogonous, C., Sha, M. K., Shiomi, K., Strong, K., Sussmann, R., Té, Y., Velazco, V. A., Vrekoussis, M., and Warneke, T.: Retrieval of greenhouse gases from GOSAT and GOSAT-2 using the FOCAL algorithm, *Atmos. Meas. Tech.*, 15, 3401–3437, <https://doi.org/10.5194/amt-15-3401-2022>, 2022.
- 530 Notholt, J., Petri, C., Warneke, T., Deutscher, N. M., Palm, M., Buschmann, M., Weinzierl, C., Macatangay, R. C., and Grupe, P.: TCCON data from Bremen, Germany, Release GGG2014.R0. TCCON data archive, hosted by CaltechDATA, California Institute of Technology, <https://doi.org/10.14291/tcon.ggg2014.bremen01.r0/1149275>, 2014.
- 535 Notholt, J., Warneke, T., Petri, C., Deutscher, N. M., Weinzierl, C., Palm, M., and Buschmann, M.: TCCON data from Ny-Ålesund, Spitzbergen, Norway, Release GGG2014.R0. TCCON data archive, hosted by CaltechDATA, California Institute of Technology, <https://doi.org/10.14291/tcon.ggg2014.nyalesund01.r0/1149278>, 2017.
- Petri, C., Rousogonous, C., Warneke, T., Vrekoussis, M., Sciare, S., and Notholt, J.: TCCON data from Nicosia, Cyprus, Release GGG2014.R0. TCCON data archive, hosted by CaltechDATA, California Institute of Technology,
- 540 <https://doi.org/10.14291/tcon.ggg2014.nicosia01.R0>, 2020.
- Rose, J. J., Xu, Q., Wang, L., and Gladwin, M. T.: Shining a Light on Carbon Monoxide Poisoning, *American Journal of Respiratory and Critical Care Medicine*, 192, 1145–1147, <https://doi.org/10.1164/rccm.201508-1579ED>, 2015.
- Rozanov, V. V., Buchwitz, M., Eichmann, K.-U., de Beek, R., and Burrows, J. P.: SCIATRAN - a new radiative transfer model for geophysical applications in the 240–2400 nm spectral region: The pseudo-spherical version, *Adv. Space Res.*, 29, 1831–1835, 2002.
- 545 Rozanov, V. V., Rozanov, A. V., Kokhanovsky, A. A., and Burrows, J. P.: Radiative transfer through terrestrial atmosphere and ocean: Software package SCIATRAN, *J. Quant. Spectrosc. Radiat. Transfer*, 133, 13–71, <https://doi.org/10.1016/j.jqsrt.2013.07.004>, 2014.
- Schneising, O., Buchwitz, M., Reuter, M., Heymann, J., Bovensmann, H., and Burrows, J. P.: Long-term analysis of carbon dioxide and methane column-averaged mole fractions retrieved from SCIAMACHY, *Atmos. Chem. Phys.*, 11, 2863–2880, <https://doi.org/10.5194/acp-11-2863-2011>, 2011.
- 550 Schneising, O., Buchwitz, M., Reuter, M., Bovensmann, H., Burrows, J. P., Borsdorff, T., Deutscher, N. M., Feist, D. G., Griffith, D. W. T., Hase, F., Hermans, C., Iraci, L. T., Kivi, R., Landgraf, J., Morino, I., Notholt, J., Petri, C., Pollard, D. F., Roche, S., Shiomi, K., Strong, K., Sussmann, R., Velazco, V. A., Warneke, T., and Wunch, D.: A scientific algorithm to simultaneously retrieve carbon monoxide and methane from TROPOMI onboard Sentinel-5 Precursor, *Atmos. Meas. Tech.*, 12, 6771–6802, <https://doi.org/10.5194/amt-12-6771-2019>, 2019.
- 555 Sherlock, V., Connor, B., Robinson, J., Shiona, H., Smale, D., and Pollard, D. F.: TCCON data from Lauder, New Zealand, 125HR, Release GGG2014.R0. TCCON data archive, hosted by CaltechDATA, California Institute of Technology, <https://doi.org/10.14291/tcon.ggg2014.lauder02.r0/1149298>, 2014.
- Shiomi, K., Kawakami, S., Ohyama, H., Arai, K., Okumura, H., Taura, C., Fukamachi, T., and Sakashita, M.: TCCON data from Saga, Japan, Release GGG2014.R0. TCCON data archive, hosted by CaltechDATA, California Institute of Technology,
- 560 <https://doi.org/10.14291/tcon.ggg2014.saga01.r0/1149283>, 2014.
- Strong, K., Roche, S., Franklin, J. E., Mendonca, J., Lutsch, E., Weaver, D., Fogal, P. F., Drummond, J. R., Batchelor, R., and Lindenmaier, R.: TCCON data from Eureka, Canada, Release GGG2014.R3. TCCON data archive, hosted by CaltechDATA, California Institute of Technology, <https://doi.org/10.14291/tcon.ggg2014.eureka01.r3>, 2019.



- Sussmann, R. and Rettinger, M.: TCCON data from Garmisch, Germany, Release GGG2014.R2. TCCON data archive, hosted by CaltechDATA, California Institute of Technology, <https://doi.org/10.14291/tcon.ggg2014.garmisch01.r2>, 2018.
- 565 Suto, H., Kataoka, F., Kikuchi, N., Knuteson, R. O., Butz, A., Haun, M., Buijs, H., Shiomi, K., Imai, H., and Kuze, A.: Thermal and near-infrared sensor for carbon observation Fourier transform spectrometer-2 (TANSO-FTS-2) on the Greenhouse gases Observing SATellite-2 (GOSAT-2) during its first year in orbit, *Atmos. Meas. Tech.*, 14, 2013–2039, <https://doi.org/10.5194/amt-14-2013-2021>, 2021.
- Tayebi, M., Naderi, M., Mohammadi, J., and Tayebi, M. H.: Comparing different statistical models for assessing Fe-contaminated soils based on VNIR/SWIR spectral data, *Environ. Earth Sci.*, 76, 734, <https://doi.org/10.1007/s12665-017-7058-y>, 2017.
- 570 Te, Y., Jeseck, P., and Janssen, C.: TCCON data from Paris, France, Release GGG2014.R0. TCCON data archive, hosted by CaltechDATA, California Institute of Technology, <https://doi.org/10.14291/tcon.ggg2014.paris01.R0/1149279>, 2014.
- United States Geological Survey: Digital Elevation - Global Multi-resolution Terrain Elevation Data 2010 (GMTED2010), <https://doi.org/10.5066/F7J38R2N>, 2018.
- 575 Veefkind, J. P., Aben, I., McMullan, K., Förster, H., de Vries, J., Otter, G., Claas, J., Eskes, H. J., de Haan, J. F., Kleipool, Q., van Weele, M., Hasekamp, O., Hoogeveen, R., Landgraf, J., Snel, R., Tol, P., Ingmann, P., Voors, R., Kruizinga, B., Vink, R., Visser, H., and Levelt, P. F.: TROPOMI on the ESA Sentinel-5 Precursor: A GMES mission for global observations of the atmospheric composition for climate, air quality and ozone layer applications, *Remote Sensing of Environment*, 120, 70–83, <https://doi.org/10.1016/j.rse.2011.09.027>, 2012.
- Warneke, T., Messerschmidt, J., Notholt, J., Weinzierl, C., Deutscher, N. M., Petri, C., and Grupe, P.: TCCON data from 580 Orléans, France, Release GGG2014.R0. TCCON data archive, hosted by CaltechDATA, California Institute of Technology, <https://doi.org/10.14291/tcon.ggg2014.orleans01.r0/1149276>, 2014.
- Wennberg, P. O., Wunch, D., Roehl, C. M., Blavier, J.-F., Toon, G. C., and Allen, N. T.: TCCON data from California Institute of Technology, Pasadena, California, USA, Release GGG2014.R1. TCCON data archive, hosted by CaltechDATA, California Institute of Technology, <https://doi.org/10.14291/tcon.ggg2014.pasadena01.r1/1182415>, 2015.
- 585 Wennberg, P. O., Roehl, C. M., Blavier, J.-F., Wunch, D., Landeros, J., and Allen, N. T.: TCCON data from Jet Propulsion Laboratory, Pasadena, California, USA, Release GGG2014.R1. TCCON data archive, hosted by CaltechDATA, California Institute of Technology, <https://doi.org/10.14291/tcon.ggg2014.jpl02.r1/1330096>, 2016a.
- Wennberg, P. O., Wunch, D., Roehl, C. M., Blavier, J.-F., Toon, G. C., and Allen, N. T.: TCCON data from Lamont, Oklahoma, USA, Release GGG2014.R1. TCCON data archive, hosted by CaltechDATA, California Institute of Technology, 590 <https://doi.org/10.14291/tcon.ggg2014.lamont01.r1/1255070>, 2016b.
- Wennberg, P. O., Roehl, C. M., Wunch, D., Toon, G. C., Blavier, J.-F., Washenfelder, R., Keppel-Aleks, G., Allen, N. T., and Ayers, J.: TCCON data from Park Falls, Wisconsin, USA, Release GGG2014.R1. TCCON data archive, hosted by CaltechDATA, California Institute of Technology, <https://doi.org/10.14291/tcon.ggg2014.parkfalls01.r1>, 2017.
- Wunch, D., Toon, G. C., Wennberg, P. O., Wofsy, S. C., Stephens, B. B., Fischer, M. L., Uchino, O., Abshire, J. B., Bernath, P., Biraud, 595 S. C., Blavier, J.-F. L., Boone, C., Bowman, K. P., Browell, E. V., Campos, T., Connor, B. J., Daube, B. C., Deutscher, N. M., Diao, M., Elkins, J. W., Gerbig, C., Gottlieb, E., Griffith, D. W. T., Hurst, D. F., Jiménez, R., Keppel-Aleks, G., Kort, E. A., Macatangay, R., Machida, T., Matsueda, H., Moore, F., Morino, I., Park, S., Robinson, J., Roehl, C. M., Sawa, Y., Sherlock, V., Sweeney, C., Tanaka, T., and Zondlo, M. A.: Calibration of the Total Carbon Column Observing Network using aircraft profile data, *Atmos. Meas. Tech.*, 3, 1351–1362, <https://doi.org/10.5194/amt-3-1351-2010>, 2010.
- 600 Wunch, D., Toon, G. C., Blavier, J.-F. L., Washenfelder, R. A., Notholt, J., Connor, B. J., Griffith, D. W. T., Sherlock, V., and Wennberg, P. O.: The Total Carbon Column Observing Network, *Phil. Trans. R. Soc. A*, 369, 2087–2112, <https://doi.org/10.1098/rsta.2010.0240>, 2011.



Wunch, D., Mendonca, J., Colebatch, O., Allen, N. T., Blavier, J.-F., Roche, S., Hedelius, J., Neufeld, G., Springett, S., Worthy, D., Kessler, R., and Strong, K.: TCCON data from East Trout Lake, Canada, Release GGG2014.R1. TCCON data archive, hosted by CaltechDATA, California Institute of Technology, <https://doi.org/10.14291/tccon.ggg2014.easttroutlake01.r1>, 2018.